ZnO−ZnS Heterojunction and ZnS Nanowire Arrays for Electricity Generation

Ming-Yen Lu,[†,‡] Jinhui Song,[†] Ming-Pei Lu,[§] Chung-Yang Lee,[‡] Lih-Juann Chen,[‡,*] and Zhong Lin Wang[†,*]

[†]School of Materials Science and Engineering, Georgia Institute of Technology, Atlanta, Georgia 30332-0245, [‡]Department of Materials Science and Engineering, National Tsing Hua University, Hsinchu, Taiwan 30043, ROC, and [§]National Nano Device Laboratories, Hsinchu, Taiwan 30078, ROC

One-dimensional semiconductor nanostructures have attracted much research interest in the past decade because of their unique properties and superior performances. Rationally designed heterojunctions in the axial,[1] radial,[2] and branch[3] direction with modulated compositions are particularly interesting for applications in solar cells,[4] high-performance field-effect transistors,[5] and versatile devices.[6,7] Lately, piezoelectric ZnO nanowire (NW) array based nanogenerators have been demonstrated.[8] ZnO NWs can effectively convert mechanical energy into electricity by utilizing its coupled effect of piezoelectric and semiconducting properties. Different kinds of integrated nanogenerators based on this principle have been demonstrated.[9−11] This significant discovery not only stimulates other potential applications of nanomaterials but also provides a new possibility for building a self-powering system in the future.[12]

As important wide band gap semiconductors, ZnO and ZnS have a wide range of applications for optical and electric devices. Recently, the studies of ZnO−ZnS heterostructures with various morphologies, such as nanorings,[13] biaxial nanowires,[14] and saw-like nanostructures,[15] have been reported. However, the synthesis of ZnO−ZnS heterojunction NW arrays remains a challenge.

In this work, we report the synthesis of axial heterostructured ZnO−ZnS NW arrays for the first time by a thermal evaporation process with the presence of residual oxygen. Furthermore, pure ZnS NW arrays have been obtained by selective etching of ZnO−ZnS NW arrays. Using the received NW arrays, we demonstrate the first application of heterostructured ZnO−ZnS and

ABSTRACT Vertically aligned ZnO−ZnS heterojunction nanowire (NW) arrays were synthesized by thermal evaporation in a tube furnace under controlled conditions. Both ZnO and ZnS are of wurtzite structure, and the axial heterojunctions are formed by epitaxial growth of ZnO on ZnS with an orientation relationship of $[0001]_{ZnO}//[0001]_{ZnS}$. Vertical ZnS NW arrays have been obtained by selectively etching ZnO−ZnS NW arrays. Cathodoluminescence measurements of ZnO−ZnS NW arrays and ZnS NW arrays show emissions at 509 and 547 nm, respectively. Both types of aligned NW arrays have been applied to convert mechanical energy into electricity when they are deflected by a conductive AFM tip in contact mode. The received results are explained by the mechanism proposed for nanogenerator.

ZnS NW arrays for converting mechanical energy into electricity. The results fully support the proposed energy converting mechanism for piezoelectric nanogenerator.[16] Cathodoluminescence properties of samples have also been discussed in detail.

RESULTS AND DISCUSSION

Figure 1a,b shows typical low- and high-magnification SEM images of samples, revealing that NWs are uniform and grown vertically from the substrate. The entire structure of NW arrays can be clearly seen from the cleaved side of samples, as shown in Figure 1c. Vertically aligned NW arrays were grown on ZnS buffer layers rather than directly on a Si substrate. The Au particles originally deposited on Si substrate may play a role as nucleation sites for the ZnS vapor depositing on the Si substrate and form a continuous film. As synthesis time increased and the supply of vapor was gradually decreased, NW arrays were grown on a ZnS buffer layer, then X-ray diffraction (XRD) was used to examine the crystal structures of samples, and the spectrum is shown in Figure 1d. There are two sets of peaks appearing in the XRD spectrum; one is
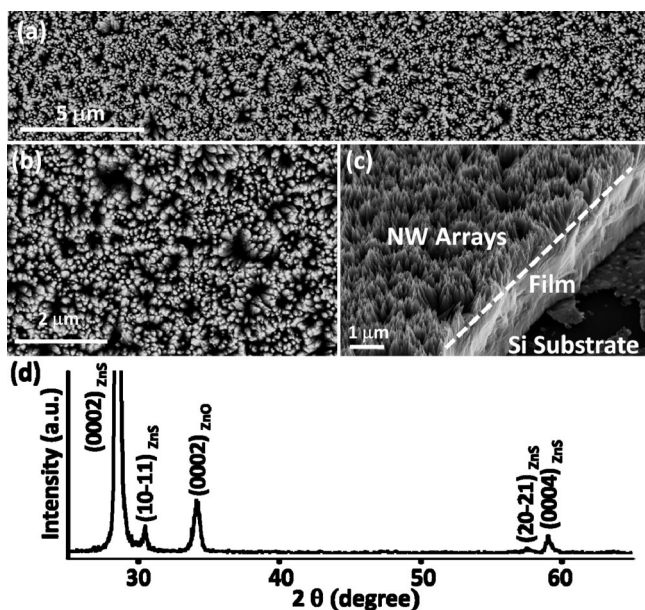
Figure 1. Structure of ZnO−ZnS heterojuction NW arrays. (a,b) Low- and high-magnification SEM images of the NW arrays, respectively. (c) Tilted SEM image revealing that NW arrays are grown vertically on a buffer layer. (d) Typical XRD pattern of the sample indicating the presence of wurtzite ZnS and ZnO.
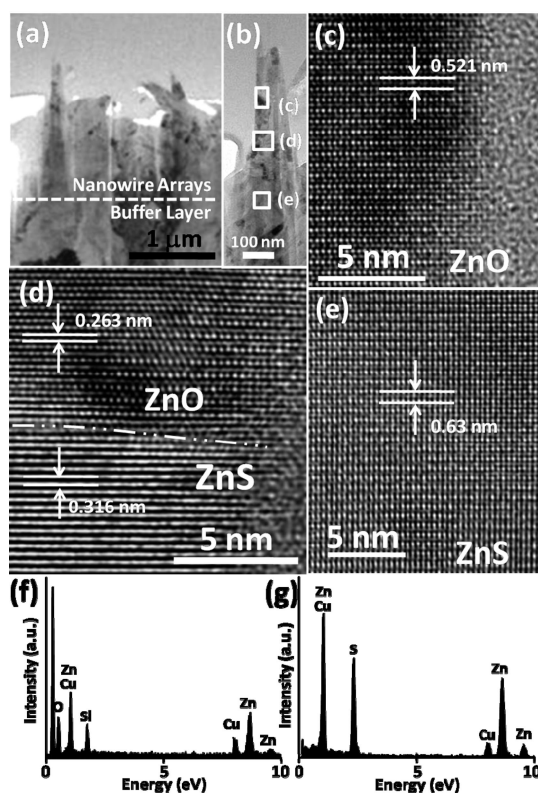

Figure 2. Structure of ZnO−ZnS heterojuction NW arrays. (a) Low-magnification XTEM image of the whole structure. (b) Magnified TEM image of a NW. (c−e) Atomic resolution TEM images from the top part, interface, and bottom part of a ZnO−ZnS heterostructure NW enlarged from the rectangular areas outlined in b, respectively. (f,g) Corresponding EDS spectra acquired from top part and bottom part of the NW, showing local compositions of ZnO and ZnS, respectively.

wurtzite structured ZnS (W-ZnS), and the other is wurtzite structured ZnO (W-ZnO). Considerably strong peak corresponding to the (0002) plane of W-ZnS indicates preferred orientation of ZnS NWs and buffer layer. Weak ZnO peaks in the spectrum represent small amounts of ZnO present in samples, which may be produced by residual oxygen during the synthesis process.

The detailed crystal structures and compositions of NW arrays were further investigated using transmission electron microscopy (TEM) and energy-dispersive X-ray spectroscopy (EDS). Low-magnification and enlarged cross-section TEM (X-TEM) images of NW arrays are shown in Figure 2a,b, indicating NWs are grown vertically on the buffer layer. Figure 2c−e shows the atomic resolution images of three distinguished segments of a single NW, as marked with rectangles in Figure 2b, to map out the distribution of crystal structures. Figure 2c,e is taken from the top and bottom parts of the NW; the lattice fringes are 0.521 and 0.63 nm, which correspond to the (0002) plane of W-ZnO and ZnS, respectively. The most striking part is the interface segment of ZnO and ZnS, as shown in Figure 2d. Lattice fringes with separations of 0.263 nm at the top part and 0.316 nm at bottom part of this figure are observed, revealing that they are W-ZnO and ZnS, respectively. Moreover, an epitaxial growth of ZnO above ZnS NW is observed at the interface. It can also be seen that a thin intermediate layer is found between, which is due to the large lattice mismatch between ZnO and ZnS. The epitaxial relationship of ZnO and ZnS can be further identified as $(0001)_{ZnO}//(0001)_{ZnS}$, $(01-10)_{ZnO}//(01-10)_{ZnS}$, and $[2-1-10]_{ZnO}//[2-1-10]_{ZnS}$, identical crystal orientation. EDS data were collected from two selected areas along a NW, as labeled with rectangles of c and e in Figure 2b, and the spectra are shown in Figure 2f,g, respectively. The results show that the top part of the NW mainly consists of Zn and O, and the bottom part of the NW is composed of only Zn and S, revealing that they are ZnO and ZnS, respectively. The Si signal in Figure 2f may originate from contamination during XTEM sample preparation. Thus, both TEM and EDS results consistently prove the formation of ZnO−ZnS axial heterojunction NW arrays.

Piezoelectric responses of the ZnO−ZnS NW arrays were examined using AFM in contact mode. The experimental setup is the same as first used for demonstrating the piezoelectric nanogenerator (NG).[8] The AFM tip scanned across the sample to deflect NWs and the output electrical signals were monitored continuously across an external load. The topography (red curve with the solid square) and voltage output (blue curve with the hollow square) line profiles recorded from one scan process are shown in Figure 3a, illustrating the electrical current generating process. The output voltage image shown in Figure 3b was recorded simultaneously when the AFM tip was scanned over the aligned NW arrays, and the scan area was 30×30 μm².

Each peak represents an electric voltage/current that was generated by deflecting the corresponding NW, and output voltages were around 6 mV. The negative signals indicate that accumulated electron charges flow from the compressed side of the NW into the Pt-coated AFM tip. According to TEM results, ZnO is at the top part of the NW arrays by epitaxial growth on ZnS NW arrays. Therefore, the voltage outputs of NW arrays mainly result from the interaction between W-ZnO and the Pt tip, and consequently, the magnitude of voltage output is in the same range as that for ZnO NW.[8] By comparing the profiles of the topological image and the output voltage image in Figure 3a, no voltage output was detected if the tip started to deflect the NW. Once the tip scanned across the NW's top and reached the compressed side of the NW, an obvious negative voltage signal was observed. Then, the signal disappeared when the NW was released by the AFM tip.

On the other hand, vertical ZnS NW arrays can be successfully obtained by removing ZnO parts of ZnO/ZnS NW arrays with dilute KOH solution. Figure 4a,b shows the top-view and side-view SEM images of pure ZnS NW arrays, respectively. Vertical morphology of NWs is still maintained, and ZnS surfaces are also slightly damaged after the selective etching process. In addition, the XRD pattern of ZnS NW arrays is shown in Figure 4c, in which all peaks can be indexed to typical W-ZnS. This result shows that the ZnO parts are substantially removed from ZnO/ZnS NW arrays, and the remaining is pure ZnS NW arrays.

Like ZnO, W-ZnS is also piezoelectric and can be used for generating electric power under mechanical stress. The piezoelectric properties of ZnS NW arrays were measured using AFM under the same conditions as for ZnO−ZnS NW arrays. Although quasi-aligned ZnS NWs have been reported previously by Lu *et al.*,[17] the piezoelectric responses of ZnS NW arrays were measured in this work for the first time. The topography (red curve with the solid square) and voltage output (blue curve with the hollow square) line profiles of ZnS NW arrays shown in Figure 5a provide strong evidence for charge accumulation and release processes when deflecting a ZnS NW. The topography and the corresponding output voltage images recorded by AFM tip when scanned over the NW arrays across an area of 20 × 20 μm² are shown in Figure 5b,c, respectively, revealing that the sharp output peaks are uniformly distributed and have similar magnitude of around 2 mV. The output signal is significantly lower than that for ZnO because ZnS has smaller piezoelectric constants and the NWs are shorter.[18]

The physical principle for creating electric potential in the NWs arises from the materials' piezoelectric property; an effective charge
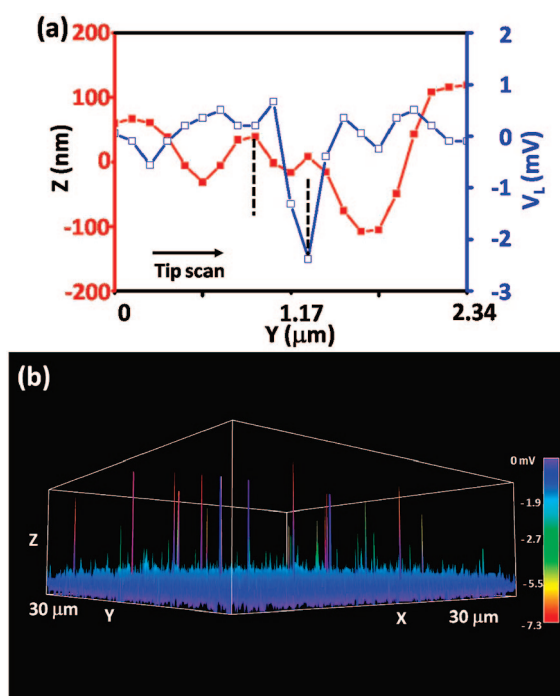
Figure 3. Application of ZnO−ZnS heterojuction NW arrays for energy generation. (a) Topography (red curve with the solid square) and voltage output (blue curve with the hollow square) line profiles across a heterostructure ZnO−ZnS NW array received by a conductive AFM tip. (b) Three-dimensional output of the voltage output image received from the AFM scan across a heterostructure ZnO−ZnS NW array with an area of 30 × 30 μm².

accumulation and output is governed by its semiconductive property and Schottky contact with the tip, as proposed previously for ZnO[8] and CdS NW.[19] The strain field across the NW is created as the AFM tip touched and started to deflect the NW; a positive piezoelectric potential (V_s^+) owing to the polarization of the charged
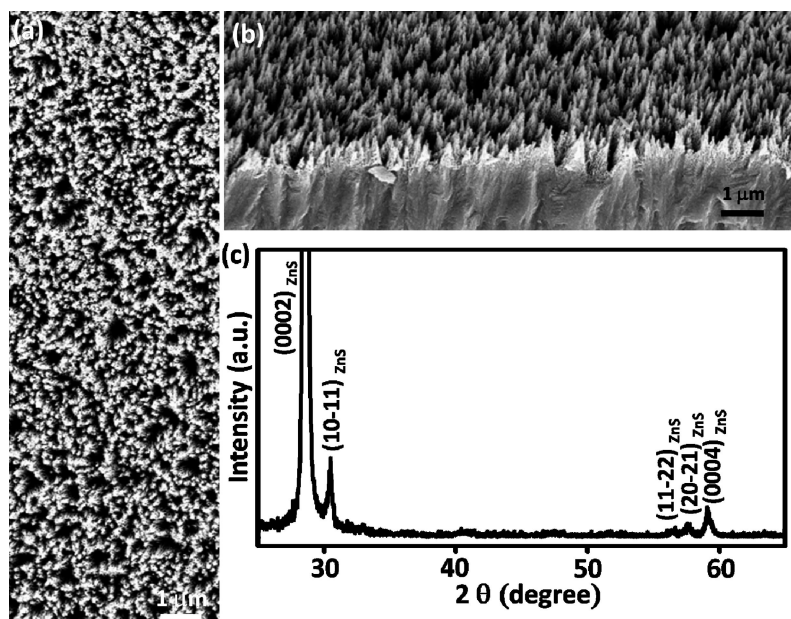
Figure 4. Structure of ZnS NW arrays. (a,b) Top-view and tilted-view SEM images of ZnS NW arrays, respectively. (c) XRD pattern of ZnS NW arrays.
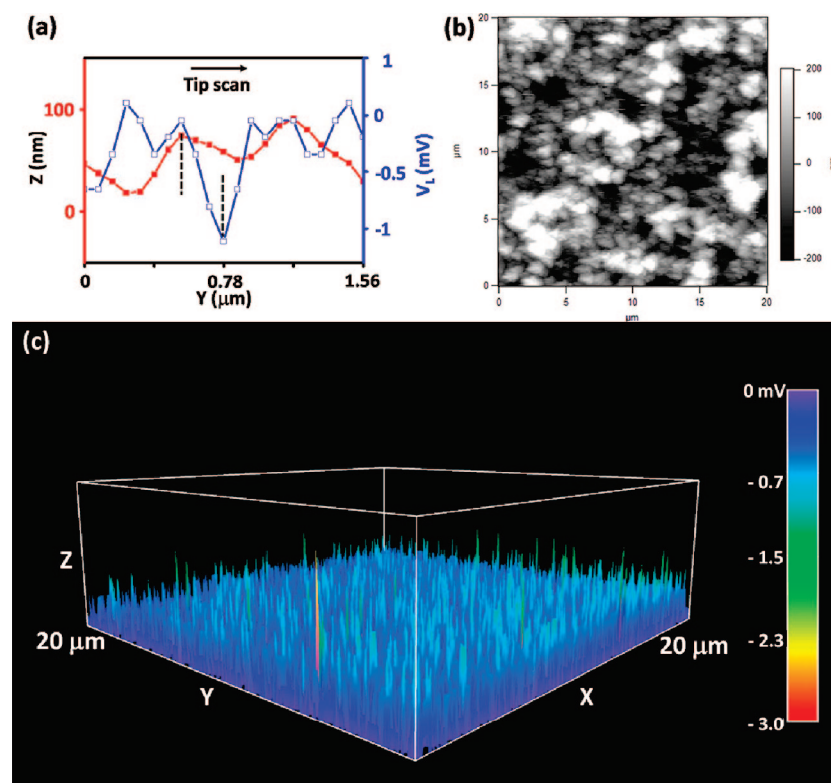
Figure 5. Application of ZnS NW arrays for energy generation. (a) Topography (red curve with the solid square) and voltage output (blue curve with the hollow square) line profiles across ZnS NW arrays. **(b,c)** Topography and the corresponding output voltage images were recorded simultaneously, respectively, when the AFM tip was scanned over the aligned ZnS NW arrays.
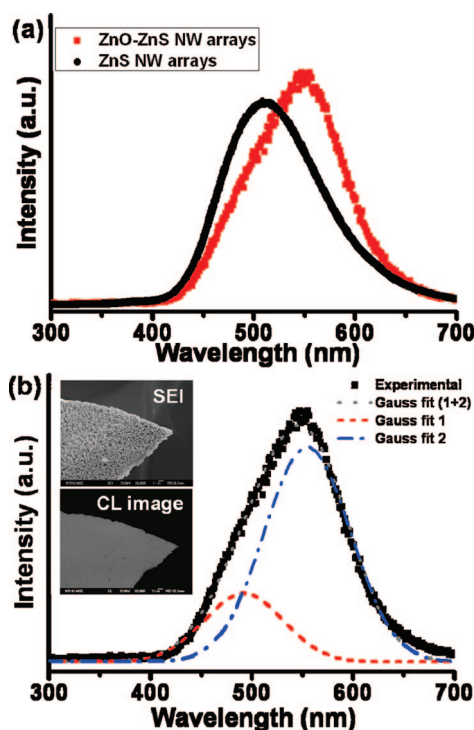

Figure 6. (a) Room-temperature CL spectra of ZnO−ZnS NW arrays and ZnS NW arrays. **(b)** Multipeak Gaussian fitting of the received CL spectra. Blue-green and green emissions are contributed from ZnS and ZnO, respectively. The inset shows the SEM image and the corresponding CL image of ZnO−ZnS NW arrays.

ions is produced at the tensile surface, and a negative piezoelectric potential (V_s^-) is induced at the compressed surface. Since the electron affinities (E_a) of ZnO and ZnS are 4.5 and 3.9 eV,[20] respectively, the work function (ϕ) of Pt is 6.1 eV, and the metal−semiconductor (M−S) interface (Pt−ZnO or Pt−ZnS) is a Schottky barrier that dominates the entire transport process. The Pt metal tip has a potential nearly zero ($V_m = 0$), while the tip is in contact with the tensile surface of the NW, so the interface of Pt and the tensile surface of the NW is negatively biased for $\Delta V = V_m - V_s^+ < 0$. In this case, the M−S interface is a reverse-biased Schottky diode. Then, the Pt tip scans across the NW and touches the compressed surface, and the M−S interface turns to the forward-biased Schottky diode due to a positively biased interface of Pt and semiconductor ($\Delta V = V_m - V_s^+ > 0$). The electric current is created by the flow of electrons in the external circuit as driven by the piezoelectric potential.[21] The observed output voltage is the difference in Fermi level between the AFM tip and the grounded side of the NW. Details of the energy generation mechanism has been presented in ref 12.

Cathodoluminescence (CL) is a useful technique for investigating the optical properties of nanostructures. Room-temperature cathodoluminescence spectra of samples are shown in Figure 6a. The CL peaks for the ZnS NW arrays and ZnO−ZnS NW arrays are centered at 509 and 549 nm, respectively. In the literature, the luminescence at 509 nm of ZnS was proposed due to Cu or Au impurities.[22,23] Au has been employed in our synthesis, thus the blue-green emission may result from Au impurities. The emission from ZnO−ZnS NW arrays is located in the green region, with its maximum intensity centered at 549 nm. Owing to asymmetric shape of the peak, multipeak Gaussian fitting gives two Gaussian bands, and the Gaussian curve fits well to the experimental curve as shown at Figure 6b. The blue-green peak supposedly results from ZnS, and the origin of this emission was discussed above. The other peak located at 557 nm is contributed from ZnO, and the emission arises from the recombination between holes trapped at the surface defects and electrons trapped at the oxygen vacancy.[24] The inset of Figure 6b shows the SEM image and the corresponding CL image of ZnO/ZnS NW arrays. The bright area of the CL image reveals the luminescent positions, and it can be found that the main light-emitting locations are consistent with the positions of NW arrays.

In summary, we have successfully synthesized for the first time axial heterostructure ZnO−ZnS

NW arrays based on a one-step thermal evaporation method. TEM studies indicate that ZnO NWs are grown on the top of ZnS NWs *via* epitaxial growth, and the epitaxial relationship of ZnO and ZnS can be identified as $(0001)_{ZnO}//(0001)_{ZnS}$, $(01-10)_{ZnO}//(01-10)_{ZnS}$, and $[2-1-10]_{ZnO}//[2-1-10]_{ZnS}$. Moreover, ZnS NW arrays were obtained by etching ZnO−ZnS NW arrays with dilute KOH solution. Both heterostructured ZnO−ZnS NW arrays and ZnS NW arrays show the potential to be used for piezoelectric energy generation. The power generation mechanism for the two types of NWs is the same as that for ZnO-based nanogenerators.[8] In addition, cathodoluminescence measurements of ZnO−ZnS NW arrays and ZnS NW arrays show the emission at 509 and 549 nm, respectively.

EXPERIMENTAL PROCEDURES

Synthesis of ZnO−ZnS NW Arrays. The synthesis of ZnO−ZnS heterostructure NW arrays was carried out by thermal evaporating ZnS powders in a vacuum tube furnace under controlled conditions. One gram of ZnS powder was loaded in an alumina boat and placed at the center of the tube. Si wafers deposited with 15 nm Au film as substrate were placed 20.5 cm away from ZnS powders at the downstream region of the tube. After the system was evacuated to 100 mTorr for 1 h, 50 sccm high purity argon gas was kept flowing through the tube, and the pressure of the tube was controlled at 5 Torr during the whole synthesis process. Then, the furnace was heated to 800 °C at a 50 °C/min rate for 10 min, followed by heating to 1100 °C at a rate of 20 °C/min and kept at this temperature for 60 min. Furnace is naturally cooled to room temperature after the synthesis process.

Formation of ZnS NW Arrays. ZnS NW arrays were successfully obtained by etching ZnO−ZnS NW arrays with 1 M KOH solution for 120 min.

Morphology and Structure Characterization. The morphology, crystal structures, and chemical compositions of samples were characterized with T-FESEM (LEO 1530 and LEO 1550), XRD (PANalytical X'Pert PRO Alpha-1), and TEM (FEI Tecnai G2 F20).

Piezoelectric Measurements of NW Arrays. Piezoelectric measurements were performed using AFM (model MFP-3 from Asylum Research) with a conducting Pt-coated silicon tip, which has a cone angle of 70°. The rectangular cantilever of the AFM had a spring constant of 1 N/m. A constant normal force of 5 nN was maintained between the tip and NW arrays in contact mode. For the electric contact at the bottom of the NWs, silver paste was applied to connect the film on the substrate surface with the measurement circuit. The output voltage across an outside load of resistance R_L of 500 MΩ was continuously monitored as the tip scanned over the NWs. No external voltage was applied during the experiment periods.

Cathodoluminescence Measurements. Optical properties of the as-synthesized products were characterized by cathodoluminescence (CL) measurements in the FESEM, which was equipped with an electron probe microanalyzer (Shimadzu EPMA-1500) under an accelerating voltage of 15 kV at room temperature.

REFERENCES AND NOTES

1. Gudiksen, M. S.; Lauhon, L. J.; Wang, J.; Smith, D.; Lieber, C. M. Growth of Nanowire Superlattice Structures for Nanoscale Photonics and Electronics. *Nature* **2002**, *415*, 617–620.
2. Wang, K.; Chen, J.; Zhou, W.; Zhang, Y.; Yan, Y.; Pern, J.; Mascarenhas, A. Direct Growth of Highly Mismatched Type II ZnO/ZnSe Core/Shell Nanowire Arrays on Transparent Conducting Oxide Substrates for Solar Cell Applications. *Adv. Mater.* **2008**, *20*, 3248–3253.
3. Jung, Y.; Ko, D.-K.; Agarwal, R. Synthesis and Structural Characterization of Single-Crystalline Branched Nanowire Heterostructures. *Nano Lett.* **2007**, *7*, 264–268.
4. Tian, B.; Zheng, X.; Kempa, T. J.; Fang, Y.; Yu, N.; Yu, G.; Huang, J.; Lieber, C. M. Coaxial Silicon Nanowires as Solar Cells and Nanoelectronic Power Sources. *Nature* **2007**, *449*, 885–890.
5. Xiang, J.; Lu, W.; Hu, Y.; Wu, Y.; Yan, H.; Lieber, C. M. Ge/Si Nanowire Heterostructures as High Performance Field-Effect Transistors. *Nature* **2006**, *441*, 489–493.
6. Tutuc, E.; Appenzeller, J.; Reuter, M. C.; Guha, S. Realization of a Linear Germanium Nanowire p−n Junction. *Nano Lett.* **2006**, *6*, 2070–2074.
7. Thelander, C.; Nilsson, H. A.; Jensen, L. E.; Samuelson, L. Nanowire Single-Electron Memory. *Nano Lett.* **2005**, *5*, 635–638.
8. Wang, Z. L.; Song, J. Piezoelectric Nanogenerators Based on Zinc Oxide Nanowire Arrays. *Science* **2006**, *312*, 242–246.
9. Wang, X.; Song, J.; Liu, J.; Wang, Z. L. Direct-Current Nanogenerator Driven by Ultrasonic Waves. *Science* **2007**, *316*, 102–105.
10. Qin, Y.; Wang, X. D.; Wang, Z. L. Microfibre−Nanowire Hybrid Structure for Energy Scavenging. *Nature* **2008**, *451*, 809–814.
11. Xu, S.; Wei, Y.; Liu, J.; Yang, R.; Wang, Z. L. Integrated Multilayer Nanogenerator Fabricated Using Paired Nanotip-to-Nanowire Brushes. *Nano Lett.* **2008**, *8*, 4027–4032.
12. Wang, Z. L. Towards Self-Powered Nanosystems: From Nanogenerators to Nanopiezotronics. *Adv. Funct. Mater.* **2008**, *18*, 3553–3567.
13. Wu, X.; Jiang, P.; Ding, Y.; Cai, W.; Xie, S.-S.; Wang, Z. L. Mismatch Strain Induced Formation of ZnO/ZnS Heterostructured Rings. *Adv. Mater.* **2007**, *19*, 2319–2323.
14. Yan, J.; Fang, X.; Zhang, L.; Bando, Y.; Gautam, U. K.; Dierre, B.; Sekiguchi, T.; Golberg, D. Structure and Cathodoluminescence of Individual ZnS/ZnO Biaxial Nanobelt Heterostructures. *Nano Lett.* **2008**, *8*, 2794–2799.
15. Shen, G.; Chen, D.; Lee, C. J. Hierarchical Saw-like ZnO Nanobelt/ZnS Nanowire Heterostructures Induced by Polar Surfaces. *J. Chem. Phys. B* **2006**, *110*, 15689–15693.
16. Wang, Z. L. Nanopiezotronics. *Adv. Mater.* **2007**, *19*, 889–892.
17. Lu, H. Y.; Chu, S. Y.; Chang, C. C. Synthesis and Optical Properties of Well-Aligned ZnS Nanowires on Si Substrate. *J. Cryst. Growth* **2005**, *280*, 173–178.
18. Xin, J.; Zheng, Y.; Shi, E. Piezoelectricity of Zinc-Blende and Wurtzite Structure Binary Compounds. *Appl. Phys. Lett.* **2007**, *91*, 112902-1–112902-3.
19. Lin, Y.-F.; Song, J.; Ding, Y.; Lu, S.-Y.; Wang, Z. L. Piezoelectric Nanogenerator Using CdS Nanowires. *Appl. Phys. Lett.* **2008**, *92*, 022105-1–022105-3.
20. Yang, Y.; Xue, S.; Liu, S.; Huang, J.; Shen, J. Fabrication and Characteristics of ZnS Nanocrystals/Polymer Composite Doped with Tetraphenylbenzidine Single Layer Structure Light-Emitting Diode. *Appl. Phys. Lett.* **1996**, *69*, 377–379.
21. Song, J. H.; Zhou, J.; Wang, Z. L. Piezoelectric and Semiconducting Dual-Property Coupled Power Generating Process of a Single ZnO Belt/Wire—A Technology for Harvesting Electricity from the Environment. *Nano Lett.* **2006**, *6*, 1656–1662.
22. Xu, S. J.; Chua, S. J.; Liu, B.; Gan, L. M.; Chew, C. H.; Xu, G. Q. Luminescence Characteristics of Impurities—Activated ZnS Nanocrystals Prepared in Microemulsion with Hydrothermal Treatment. *Appl. Phys. Lett.* **1998**, *73*, 478–480.

23. Xiong, Q. H.; Chen, G.; Acord, J. D.; Liu, X.; Zengel, J. J.; Gutierrez, H. R.; Redwing, J. M.; Lew Yan Voon, L. C.; Lassen, B.; Eklund, P. C. Optical Properties of Rectangular Cross-Sectional ZnS Nanowires. *Nano Lett.* **2004**, *4*, 1663–1668.

24. Hsu, N. E.; Hung, W. K.; Chen, Y. F. Origin of Defect Emission Identified by Polarized Luminescence from Aligned ZnO Nanorods. *J. Appl. Phys.* **2004**, *96*, 4671–4673.